

Versatile fiber-coupled system for simultaneous photon correlation spectroscopy and Fabry–Perot interferometry

R. B. Bogoslovov,^{a)} D. P. Shelton, J. C. Selser, G. Piet, and S. Peng
Department of Physics, University of Nevada, Las Vegas, Las Vegas, Nevada 89154-4002

(Received 17 February 2004; accepted 15 July 2004; published 20 September 2004)

We demonstrate an experimental setup utilizing fiber-optic detection and coupling of scattered light into existing photon correlation spectroscopy (PCS) and Fabry–Perot (F–P) interferometry systems. The performance of the fiber coupled F–P as a high-resolution interferometer is considered in detail. Several practical issues and limitations are discussed, including the selection of optic and fiber-optic components, collimation, effects of the fiber mode structure and core diameter, and alignment issues. A series of test measurements on standard systems with well known properties shows that the proposed fiber-optic design meets the performance expectations for both PCS and F–P instruments and presents an attractive alternative to the classical pinhole design. © 2004 American Institute of Physics. [DOI: 10.1063/1.1790561]

I. INTRODUCTION

Laser light scattering techniques have been widely used to study liquid phase dynamics (Fig. 1). The individual techniques cover a broad range of frequencies and are complementary to each other. Rotational and vibrational dynamics give rise to Raman scattering and are typically studied by traditional grating spectrometers. The propagation of acoustic waves results in Brillouin scattering and is analyzed using Fabry–Perot (F–P) interferometers. Diffusion in suspension and collective phenomena are studied by quasi-elastic light scattering using photon correlation spectroscopy (PCS). The rapid development of fiber-optic technologies has made it possible to combine different light scattering techniques in a multi-instrument experimental setup allowing for simultaneous or consecutive measurements without changing the experimental conditions or disturbing the sample system between different measurements. The greatest advantage of the fiber-optic approach is the flexibility of the experimental setup featuring a very broad dynamic range, having access to various scattering angles and the ability to be expanded and include any number of additional instruments. Moreover, this approach can be easily implemented in high-pressure experiments or used with miniature volume samples and can be adapted to perform measurements in industrial environments or in experiments that require remote detection.

Multimode fibers and fiber bundles have been commonly used for coupling scattered light to grating spectrometers.¹ In the field of PCS, it was shown by Brown² and by Rička^{3,4} that single-mode fiber detection results in superior quality of the collected autocorrelation functions as compared to a classical two pinhole detection or multimode fiber detection schemes. The improvement yields higher coherence factors while maintaining sufficient light-collection efficiencies. The method is gaining popularity and there is at least one commercial system (ALV-Laser Vertriebsgesellschaft mbH,

Langen/Hessen, Germany) implementing the idea. Our literature survey revealed that there is very little information on the use of fiber-optics in Brillouin scattering experiments implementing high-resolution plane-parallel F–P interferometers. Pakulski and Holuj⁵ describe an experimental setup using a 200 μm multimode fiber along with a triple-pass F–P, but their attention was focused on the automated stabilization procedure they developed. To the best of our knowledge, single-mode fiber detection has not yet been used as a coupling scheme for high-resolution F–P interferometry.

In this article, we describe an experimental setup implementing fiber-optic coupling and combining PCS and F–P interferometry. The setup affords access to a very broad dynamic range—some 15 orders of magnitude in frequency. We focus our discussion mainly on the F–P interferometer since fiber-optic detection for PCS is considered in detail elsewhere.^{3,4} In the following section, we introduce some basic definitions and relations which are necessary to address the performance of the proposed fiber-optic experimental setup and allow for a comparison with the classical pinhole detection. Section III describes the experimental setup. Next, we address a variety of practical design issues including the selection of optic and fiber-optic components, collimation, effects of the fiber mode structure and core diameter, alignment issues, etc. In Sec. IV, we present results of test measurements of the F–P performance with various multimode fibers and demonstrate that the reduction in the resolution with increased fiber size is due to the increased size of the effective entrance aperture of the instrument and not to the mode structure of the fiber. Next, we present Brillouin spectra of toluene and *n*-hexadecane and PCS measurements of molten poly(ethylene oxide), (PEO) both obtained with the single-mode fiber detection setup. We offer qualitative and quantitative comparisons between the fiber-optic and the classic pinhole systems.

^{a)}Electronic mail: radoslav@physics.unlv.edu

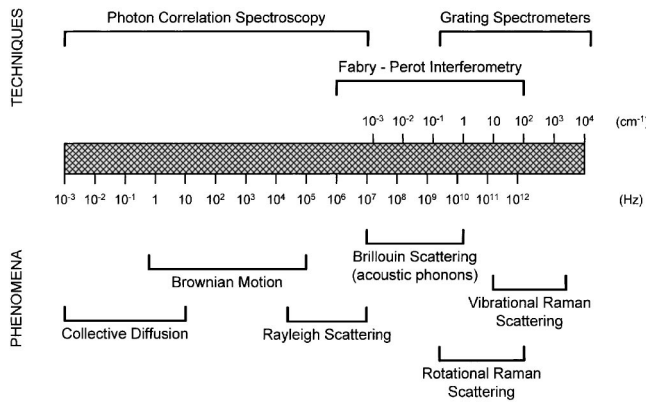


FIG. 1. Laser spectroscopy.

II. THEORY AND BACKGROUND

A. Fabry-Perot interferometer

The classical plane-parallel F-P interferometer is schematically shown in Fig. 2(a). The sample is illuminated by a laser beam in a typical light scattering geometry. Single-mode operation of the laser is essential, and it is usually achieved by introducing an etalon inside the laser resonator. The scattered light from the sample is collimated by the first lens, L_1 and then passed through the two parallel F-P mirror plates with adjustable spacing, d . For simplicity, we assume a refractive index $n=1$ (air-filled mirror spacing), normal incidence, and negligible absorption. The second lens, L_2 collects the light and the output signal is detected through a pinhole with diameter a_2 which selects only rays incident on the F-P within a narrow angular range. The diameter of the preimage of the pinhole a_2 and the size of the illuminating laser beam determine the scattering volume in the sample. When an optical fiber delivers the signal to the input of the interferometer [Fig. 2(b)], the only difference is that the an-

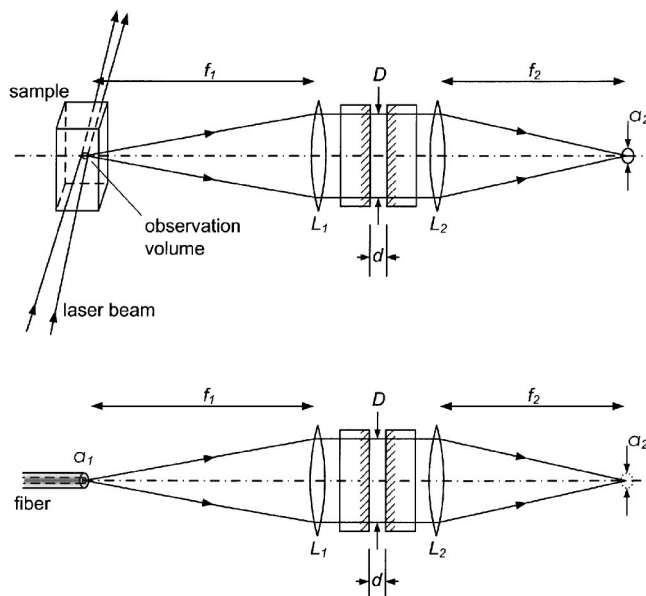


FIG. 2. (a) Classic (pinhole) and (b) fiber-coupled plane-parallel F-P interferometer. Collimating lens L_1 with focal length f_1 . Detector lens L_2 with focal length f_2 . D —mirror aperture; d —adjustable mirror spacing.

gular selection is performed with the fiber core of diameter a_1 serving as the limiting aperture.

The theory of operation and the transfer function of the F-P interferometer are described in many textbooks⁶⁻⁸ and will not be repeated here. The transmittance function is periodic with maxima occurring when an interference condition is fulfilled. Two adjacent interference orders are separated by a frequency interval called the free spectral range (FSR) (measured in Hz)

$$\Delta\nu_{FSR} = \frac{c}{2d}, \tag{1}$$

where c is the speed of light in a vacuum. Two properties are characteristic for the transmission function: The full width at half maximum (FWHM), $\Delta\nu_{FWHM}$ and the suppression of light between the maxima, measured by the contrast, $C = I_{max}/I_{min}$

$$C = \frac{(1 + R)^2}{(1 - R)^2}, \tag{2}$$

with R being the reflectance (defined for light intensity) of the F-P mirror plates.

The ratio of the peak separation to the FWHM width of a peak defines the finesse of the instrument

$$F = \frac{\Delta\nu_{FSR}}{\Delta\nu_{FWHM}}. \tag{3}$$

In the ideal case considered so far, assuming no absorption, perfect flatness of the two reflecting surfaces and perfectly collimated illumination beam, corresponding to infinitely small aperture a_1 and ideal lens system, the finesse depends only on the reflectivity. It is often referred to as the reflectivity finesse

$$F_R = \frac{\pi\sqrt{R}}{1 - R}. \tag{4}$$

In a real instrument, one has to consider the effects of imperfect reflecting surfaces, finite aperture size, monochromatic aberrations of the collimating optics, etc. All of these imperfections lower the finesse and the instrument's resolution. The total or effective finesse is given by

$$\frac{1}{F_{eff}^2} = \frac{1}{F_R^2} + \frac{1}{F_M^2} + \frac{1}{F_A^2} + \dots \tag{5}$$

The two most significant corrections are given by the flatness finesse

$$F_M = \frac{M}{2}, \tag{6}$$

with M being the flatness figure for the mirror's surface with root-mean-square (rms) flatness λ/M , and the aperture (pinhole) finesse

$$F_A = \frac{\lambda}{d} \frac{4f_1^2}{a_1^2}, \tag{7}$$

with f_1 being the focal length of the collimator [Fig. 2(b)]. The combination of the reflectivity and flatness finesse, $F_{RM} = (F_R^2 + F_M^2)^{-1/2}$ is a fixed parameter for a given mirror

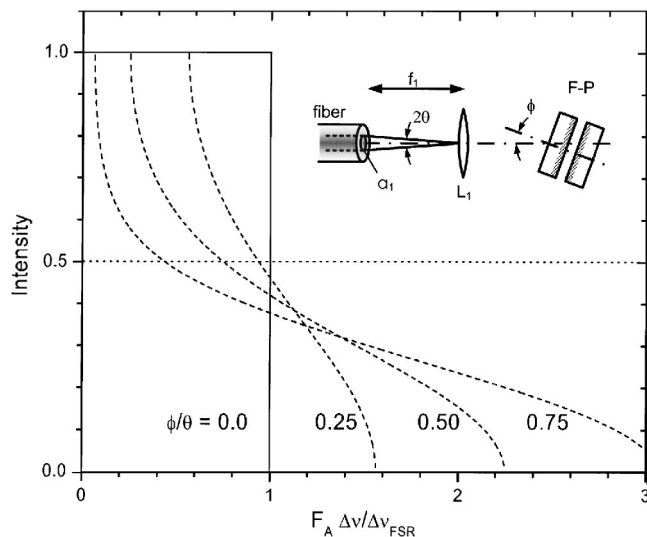


FIG. 3. Misalignment effect. ϕ —misalignment angle between collimator axis and F-P axis; θ —angular size of the fiber aperture.

set and in the case of a small fiber diameter determines the width and shape of the transmission function. The degree of collimation depends on the angular size of the fiber aperture as seen by the collimator (see also the inset in Fig. 3)

$$\theta = \frac{a_1}{2f_1}. \quad (8)$$

The angular size of the aperture a_1 can be decreased by increasing the focal length f_1 of the collimator until the beam diameter fills the entire useful aperture, D of the interferometer. When θ approaches $\sqrt{\lambda}/F_{RM}d$, the beam through the interferometer is not sufficiently collimated, F_A becomes comparable to F_{RM} , and the effective finesse is reduced according to Eq. (5).

If F_A is much lower than F_{RM} , the transmission is dominated by the fiber aperture and it is strongly dependent on the mutual alignment between the collimator axis and the interferometer axis. In the limit $F_A \gg F_{RM}$ and perfect alignment, the transmission peak will have the rectangular shape shown by the solid line in Fig. 3. However, if the two axes are misaligned by angle ϕ , the line shape will be deformed as shown by the dashed curves in Fig. 3 for several values of the misalignment parameter ϕ/θ . The maximum transmission remains the same but the width at half maximum decreases. Since the peaks have a long tail and are highly asymmetric, this regime is very unsuitable for spectroscopic applications. It can occur when high reflectivity mirrors and large fiber diameters are combined, as will be shown later.

B. Photon correlation spectroscopy

The technique of PCS is a standard dynamic light scattering technique.^{9–11} Fluctuations in the intensity of the scattered light provide a signature of the dynamics of the system. For example, from the scattered-light autocorrelation function (ACF), one can deduce the diffusion coefficient of particles in suspension.

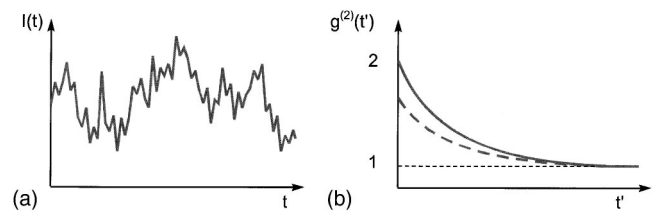


FIG. 4. PCS. (a) Intensity and (b) normalized ACF.

A correlator forms in real time the ACF between the scattered-light intensities at time t and at some later time $t + t'$ (Fig. 4), where t' is called the lag time or time shift. The normalized intensity ACF is given by

$$g^{(2)}(t') = \frac{\langle I(t)I(t+t') \rangle}{\langle I(t) \rangle^2} \quad (9)$$

Fluctuations can be observed only if the detection optics provide sufficient angular resolution. Ideally, the initial value of the ACF amounts to twice its limiting value at large values of t' (Fig. 4, solid line). In practice, the amplitude of the dynamic part of the correlation function decreases with decreasing angular resolution (Fig. 4, dashed line).

A general property of the ACF is expressed by the Siegert relation

$$g^{(2)}(t') = 1 + f|g^{(1)}(t')|^2, \quad (10)$$

with $g^{(1)}(t')$ being the ACF for the scattered electric field. The factor f in front of the dynamic part of the ACF is called the coherence factor, $0 \leq f \leq 1$. In a classical setup, consisting of a circular aperture stop at the imaging lens and a pinhole at its focus, the value of f depends on the area of the pinhole $f = f(A)$ and is typically in the range of 0.5–0.8. Generally speaking, when the scattered light has low intensity, one is forced to work with larger pinholes—which in turn leads to a lower coherence factor. If the scattering is strong, it is possible to use a smaller size pinhole thus improving the coherence factor. The signal-to-noise ratio is high when both a high coherence factor and high light-collection efficiency are achieved.

In his work, Rička³ compared the classical (pinhole) setup with a fiber-optic detection setup and showed, both theoretically and experimentally, that by using a single-mode fiber to collect and transport the light to the detector, one can achieve the theoretical limit of 1 for the coherence factor while maintaining high light-collection efficiency. Using multimode fiber results in intermediate coherence factors and, in the limit of very large number of modes, it practically converges to the coherence factor from a uniformly illuminated pinhole of the same diameter as the fiber. Therefore,

$$f_{\text{pinhole}} < f_{\text{MM fiber}} < f_{\text{SM fiber}}. \quad (11)$$

III. EXPERIMENTAL SETUP

A. Experiment layout

The experimental setup we designed and built is schematically shown in Fig. 5. We use an argon-ion laser (Coherent, Palo Alto, California) operating in a single longitudinal and transverse mode at $\lambda = 514.5$ nm. The laser output is ver-

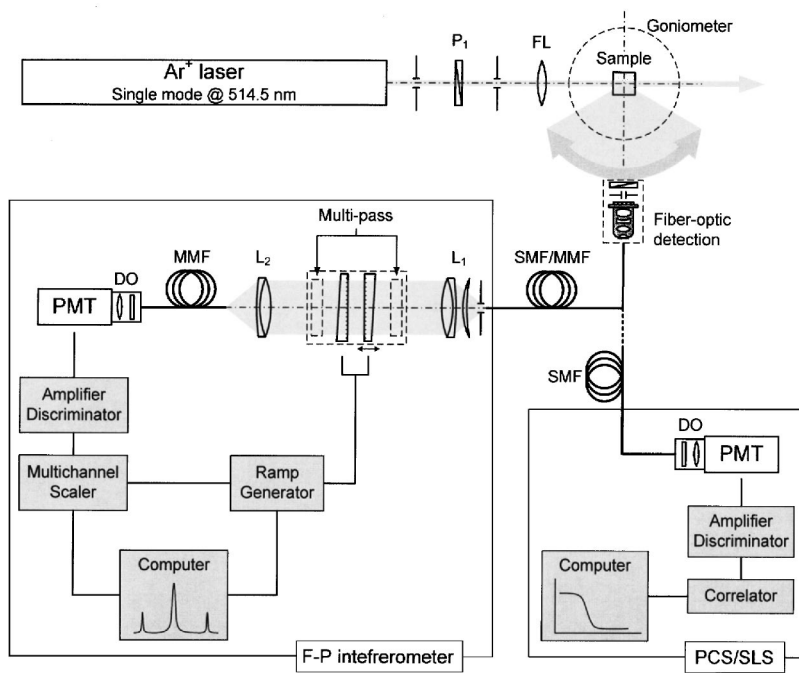


FIG. 5. Experimental setup. P_1 —polarizer; FL—focusing lens; PMT—photomultiplier tube; DO—detector optics; SMF—single-mode fiber; MMF—multimode fiber; L_1 —collimating optics; and L_2 —collecting lens. Fiber-optic detection consists of a polarizer, iris aperture, and microscope objective.

tically polarized and moderately focused at the center of the sample cell. The goniometer assembly along with the sample holder, index matching vat, and temperature control are part of a standard light-scattering setup for PCS and static light-scattering (PCS/SLS) model BI-200SM from Brookhaven Instruments Corp. (Holtsville, New York). As an index matching liquid, we use toluene. The angle of the goniometer arm is adjusted by a stepper motor. To couple the scattered light into the receiver end of the fiber, we use a microscope objective and compact five-axis spatial filter assembly both from Newport Corp. (Irvine, California), modified to accommodate standard fiber connectors in place of its pinhole. The spatial filter assembly is mounted on the goniometer arm and it provides sufficient degrees of freedom for precise alignment.

For polarization dependent measurements, a polarizer may be used in front of the optical assembly. It is essential to resolve the polarization of the scattered light before it is

coupled into the fiber since a standard optical fiber scrambles the polarization dependent information in the signal. Alternatively, a polarization preserving fiber can be used. In this case, to resolve the polarization at different orientations, the fiber has to be rotated around its axis which might lead to alignment problems.

In order to keep the setup as versatile as possible, it has to allow for easy and quick substitution of different fibers. The fibers tested with the setup along with some of their basic characteristics are listed in Table I. The first three fibers (SM-3.5, MM-4, and MM-6.6) used standard FC connectors whereas the rest of the fibers used standard SMA connectors. Most of the fiber-optic vendors allow specifying the connector type, thereby facilitating a system design having fully interchangeable fibers.

Once the scattered light is coupled into the receiving fiber it can be directed to either of the two instruments, PCS/

TABLE I. Single-mode and multimode fibers used in this work.

Fiber	SM—3.5	MM—4	MM—6.6	MM—8.2	MM—50	MM—100	MM—200	MM—400
Core diameter	3.5 μm^a	4 μm^a	6.6 μm^a	8.2 μm	50 μm	100 μm	200 μm	400 μm
Specified cutoff wavelength	430 nm	620 nm	950 nm	1260 nm
Numerical aperture	0.13	0.12	0.13	0.14	0.22	0.22	0.22	0.22
Number of modes @ 514.5 nm	1	3	6	10	~2260 ^b	~9000 ^b	~36 000 ^b	~145 000 ^b
Connector	Single mode FC	FC	FC	SMA	SMA	SMA	SMA	SMA
Supplier	Nufern (ThorLabs)	3M (ThorLabs)	3M (ThorLabs)	Ocean Optics	Ocean Optics	Ocean Optics	Ocean Optics	Ocean Optics

^aMFD—Mode field diameter.

^bEstimated.

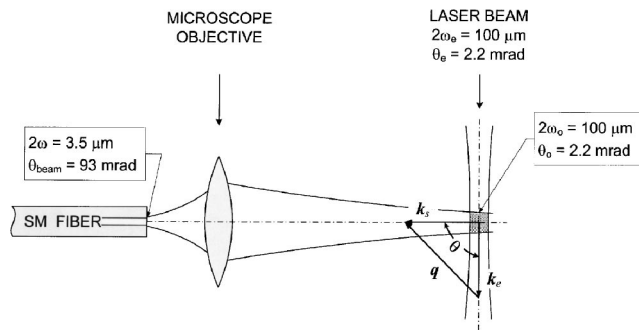


FIG. 6. Single-mode fiber detection. The half-angle divergence of the excitation and observation beams in the toluene sample, θ_e and θ_o , were calculated using the expression $\theta = \tan^{-1}(\lambda/n\pi\omega)$, with $\lambda = 514.5$ nm and refractive index $n = 1.5$. The beam divergence of the fiber mode in air ($n = 1$) is less than the numerical aperture of the fiber (0.13).

SLS or F-P interferometer, and then analyzed and stored by the appropriate electronic equipment.

The F-P interferometer used was a model RC-110 from Burleigh Instruments (now EXFO Burleigh Products Group Inc., Victor, New York). The beam leaving the receiver fiber is collimated by the first lens system, L_1 which is only schematically shown in Fig. 5. Better collimation directly results in better resolution; therefore, a good quality achromatic doublet or a more refined lens system is essential. The collimator used in our setup was a nearly aplanatic meniscus lens followed by a 2 in. achromatic doublet. After light passed through the F-P interferometer, it was collected by the second lens, L_2 , and then focused into a multimode fiber with large core diameter (typically 400 μm) and directed to the photomultiplier tube (PMT). The PMT optics consisted of a laser band-pass filter for 514.5 nm and a biconvex imaging lens.

B. Light collection and alignment

In a well-aligned system the excitation (laser) beam and the receiver (fiber) beam intersect at the center of rotation of the goniometer and lie in one plane at all angles of the goniometer arm (Fig. 6). Both beams are well approximated as Gaussian beams with wave vectors \mathbf{k}_e and \mathbf{k}_s inside the scattering volume. An angle θ between the excitation and the observation beam determines the scattering vector $\mathbf{q} = \mathbf{k}_s - \mathbf{k}_e$ with magnitude

$$|\mathbf{q}| = \frac{4\pi n}{\lambda} \sin \frac{\theta}{2}. \quad (12)$$

The geometry described can be easily visualized by coupling part of the laser beam into the back end of the receiving fiber. The two beams are clearly visible in the index matching liquid which greatly assists the initial alignment.

The choice of the optimal beam parameters is considered in detail by Rička.^{3,4} Here, we briefly summarize his conclusions. In the case of perfect alignment and the Gaussian beam approximation, the average signal at the detector is inversely proportional to the radius of the excitation beam, ω_e , and it is independent of the radius of the observation beam, ω_o [see Eq. (26) in Ref. 3]. Therefore, the light-collection efficiency increases linearly with decreasing exci-

tation beam diameter. In practice, the focusing of the laser beam is limited by the power density in the sample which leads to thermal effects. On the other hand, the observation beam can be expanded without sacrificing light-collection efficiency—by increasing the observation beam diameter, the number of observed scatterers increases quadratically, but the signal collected from each scatterer decreases correspondingly since the solid angle of the light-collection decreases. Working with a larger receiver beam diameter makes the setup less sensitive to misalignment and since the collection solid angle is smaller, the uncertainty in the scattering vector, \mathbf{q} is reduced.

It was demonstrated^{3,4,12} that good alignment and adequate light-collection efficiency in both PCS and static light scattering can be achieved by using graded index (GRIN) lenses and a receiver beam slightly focused or collimated with a beam diameter at the location of the sample in the range from 0.3 to 1 mm. As shown in Fig. 6, our setup uses a microscope objective to couple the scattered light into the single-mode fiber. In this case, both the laser and receiver beams were focused to an equal spot size about 100 μm in diameter. Even with such small beam diameters, the alignment at any fixed scattering angle was very easy. Initially, a fraction of the laser beam is coupled in the backward direction in the fiber. The beam emerging from the receiver end is then intersected with the excitation beam at the center of the index matching vat. Subsequently, the receiving fiber is connected to the PMT and fine adjustment is performed by maximizing the signal (we simply used the light scattered by the toluene in the vat), while the fiber beam is translated vertically across the excitation beam profile. Proper alignment at all scattering angles is more difficult, but not impossible. To test the alignment at different scattering angles, we used the following standard procedure: The scattering intensity from toluene, $I(\theta)$ was recorded as a function of the scattering angle, θ . Since toluene is a Rayleigh scatterer, the quantity $I(\theta)\sin(\theta)$, should be independent of scattering angle. As we tested the alignment between 20° and 150°, the quantity $I(\theta)\sin(\theta)$ (averaged over ten runs at each measured angle and corrected for dark count and dead time for the PMT) was constant to within $\pm 2.5\%$. Similarly, Suparno *et al.*¹² demonstrated alignment to within $\pm 3\%$ for scattering angles in the range from 15° to 160° using a GRIN lens and collimated receiver beam with a diameter of 800 μm .

In the case of the F-P interferometer, the ability to perform detection easily at various scattering angles and, therefore, the ability to vary the scattering vector \mathbf{q} , presents a substantial improvement over the conventional pinhole setup. Historically, angle dependent measurements with F-P interferometers were very rarely performed. The size and weight of the interferometer makes it practically impossible to be repositioned at different angles with respect to the excitation laser beam. On rare occasions, sophisticated optical designs were employed that allowed the axis of the laser beam to be rotated with respect to the stationary axis of the interferometer.¹³ These methods were difficult for implementation and alignment and have had only limited application. Due to the lack of a convenient multiangle setup, the vast majority of experiments published in literature are limited to

90° scattering angle. By contrast, the proposed fiber-optic approach facilitates experiments over a broad range of scattering angles.

C. Multimode fiber coupling to the Fabry-Perot interferometer

In some experimental situations, the scattered light from the sample has very low intensity and the detection becomes problematic. As examples, this could be the case in very dilute solutions or in small molecule liquids. In order to collect as much scattered light as possible, it would be preferable to use multimode fibers with a larger core diameter and numerical aperture in place of the single-mode fiber. It was already mentioned that in the case of PCS, using multimode fibers leads to decreased coherence factors and must be avoided if possible. On the other hand, detection from a single coherence area is not essential for the operation of the plane-parallel F-P interferometer.

The single-mode fiber and small diameter multimode fibers essentially behave as point source illumination of the F-P interferometer and do not reduce the finesse from its reflectivity-flatness value. On the other hand, the aperture finesse F_a may become the limiting factor for fibers with diameters of 50 μm and larger. Furthermore, full utilization of the large numerical aperture of a multimode fiber requires that both the F-P mirrors and the collimator operate at large aperture. In this regime, the flatness and regularity of the mirror surfaces—as well as the monochromatic aberrations of the lens—become more critical. Careful design and higher-quality elements can improve the finesse considerably, especially with large plate separations when the divergence of the illuminating beam has a greater effect.

D. Samples and preparation

To test the fiber-coupled experimental setup, we used toluene and *n*-hexadecane, both with well-known Brillouin spectra, as well as the molten polymer PEO, which was well characterized in previous PCS measurements in our lab.^{14,15} High-purity toluene (99.9% min. by gas chromatography (GC)) was supplied by Burdick & Jackson (Muskegon, Michigan). High-purity *n*-hexadecane (99.9% min. by GC) was supplied by Tokyo Chemical Industry (TCI) America Inc. (Portland, Oregon). A low molecular weight PEO sample ($M_w=1060$), designated here as “PEO-1K sample”, with a narrow molecular weight distribution ($M_w/M_N=1.03$) was custom synthesized by Polymer Standards Service (Mainz, Germany). PEO chain ends were “capped” with methyl groups to avoid complicating behavior associated with chain hydroxyl end groups. Based on rheological measurements, the PEO-1K sample is unentangled in the melt (the critical value for the melt entanglement molecular weight is about 3500) and the melting temperature is about 38 °C. After receiving the polymer samples, they were further purified, dried, and handled in a dry box under dry nitrogen. All samples were filtered through 0.2 μm pore-size Teflon membrane filters (Millipore, Bedford, Massachusetts) into dust-free 5 mm square spectrofluorometer cuvettes (Starna, Atascadero, California).

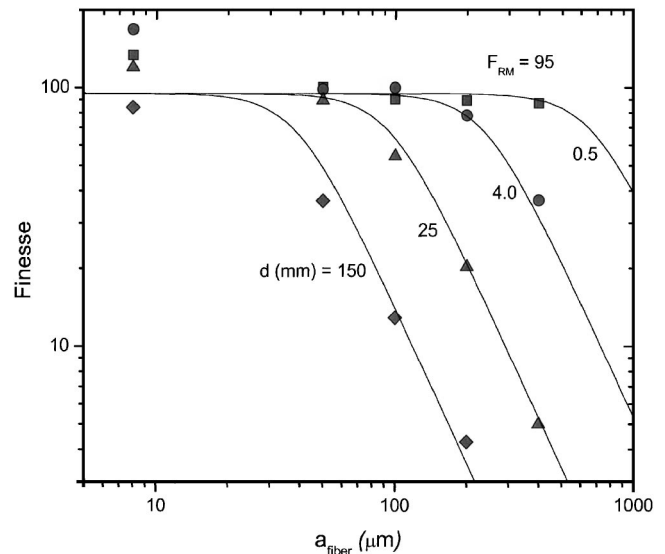


FIG. 7. Effect of the fiber core diameter on the F-P interferometer finesse. A series of curves representing the limit imposed by the instrument for various mirror separations, d . The measured values are for fibers with core diameters of 8 μm , 50 μm , 100 μm , and 200 μm .

IV. RESULTS AND DISCUSSION

A. Resolution of the fiber-coupled plane-parallel Fabry-Perot interferometer

In this measurement, we used a $\lambda=532$ nm laser beam coupled directly into the fiber, and took special care to fully and uniformly illuminate the entire fiber aperture. The fibers used had core diameters of 8 μm , 50 μm , 100 μm , 200 μm , and 400 μm (see Table I), and the collimator had 100 mm focal length and 50 mm aperture. We used a 50 mm diameter F-P mirror set with maximum measured finesse of 95 at full aperture. The reflectivity finesse was determined from measurements of the mirror reflectivity at various 2 mm diameter spots on the mirror surfaces and averaged about $F_R=156$. Thus, the inferred finesse due to surface figure and roughness was 120, corresponding to a rms surface figure error of about $\lambda/240$ for the full aperture of the F-P plates.

Figure 7 summarizes our measurements for four different separations between the F-P mirror plates $d=0.5$ mm (squares), 4.0 mm (circles), 25 mm (triangles), and 150 mm (diamonds). The solid curves on the graph are calculated using Eqs. (5) and (7). The agreement between measurement and model is very good. The 8 μm fiber results are slightly higher than the prediction due to the fact that the numerical aperture is lower resulting in a smaller beam diameter sampling a smaller surface of the F-P plates.

There are two important practical observations.

- (1) Multimode fiber coupling is equivalent to the use of an incoherently illuminated pinhole with the same diameter as the fiber core. The prediction for aperture limited finesse is not changed by the mode structure of the fiber.
- (2) In the case when the aperture finesse, F_A , is comparable to or lower than the reflectivity finesse, F_R , the shape as well as the width of the transmission function are sensitive to misalignment of the pointing of the collimator with respect to the F-P axis. The transmission peaks for

the misaligned spectrometer have a narrower apparent width and a nonsymmetrical shape, with most of the signal in a long tail. This effect is undesirable for spectroscopic applications and could be especially dangerous in combination with automated alignment routines which minimize the peak's linewidth but do not take into account the peak's shape. In Fig. 7, nice symmetrical line shapes were obtained for the points lying close to the horizontal limit set by the mirror plate's finesse (combined reflectivity and flatness), but distorted line shapes were typical for the points far below that line. It is better to use a mirror set with reflectivity finesse not too much larger than the aperture finesse, thus improving both the line shape and increasing the peak transmission of the interferometer.

B. Brillouin scattering with single-mode fiber receiver

Next, we assess the performance of the Fabry–Perot interferometer using a single-mode fiber receiver and a different set of mirror plates with reflectivity-flatness finesse of about 55. We used two reference systems, toluene and *n*-hexadecane, both widely studied with well-determined Brillouin shifts.^{8,16} Both measurements were performed at room temperature ($T=21\text{ }^{\circ}\text{C}$) with $\lambda=514.5\text{ nm}$ excitation and 90° scattering angle. The Brillouin spectra we obtained are shown in Fig. 8. The Brillouin peaks are well resolved. The observed instrument resolution was $\Delta\nu_{\text{FWHM}}\approx 300\text{ MHz}$. We used the published values for the Brillouin frequency shifts in toluene to calibrate the FSR of our F–P interferometer and determined $\Delta\nu_{\text{FSR}}\approx 17\text{ GHz}$. Therefore, the experimentally determined finesse [using Eq. (3)] was about 55–56, in agreement with the expected finesse for this mirror set. This demonstrates that the finesse is limited only by the reflectivity-flatness finesse of the mirror set and is not reduced by the introduction of the single-mode fiber detection. It was confirmed that the fiber-optic setup has stable performance in terms of very good reproducibility of the results between different measurements. In addition, the performance of the single-mode fiber detector was verified with an in-house built triple-pass feature and the results were equally good.

Since there are no published Brillouin scattering results using single-mode fiber detection, the above spectra can be compared to those obtained with the classical (pinhole) detection. Brillouin spectra of liquid toluene and various other liquids are reported by Kato and Zdasiuk¹⁶ and more recently by Rubio *et al.*¹⁷ Brillouin spectra of *n*-hexadecane are reported in many publications by Patterson (see Ref. 8 and references therein). Applying single-mode fiber detection, we obtain essentially the same results with comparable experimental resolution.

C. Photon correlation spectroscopy with single-mode fiber receiver

We performed a series of PCS measurements to test the single-mode fiber detection performance and to determine whether or not the quality of the autocorrelation function follows the prediction outlined in the theoretical section. In

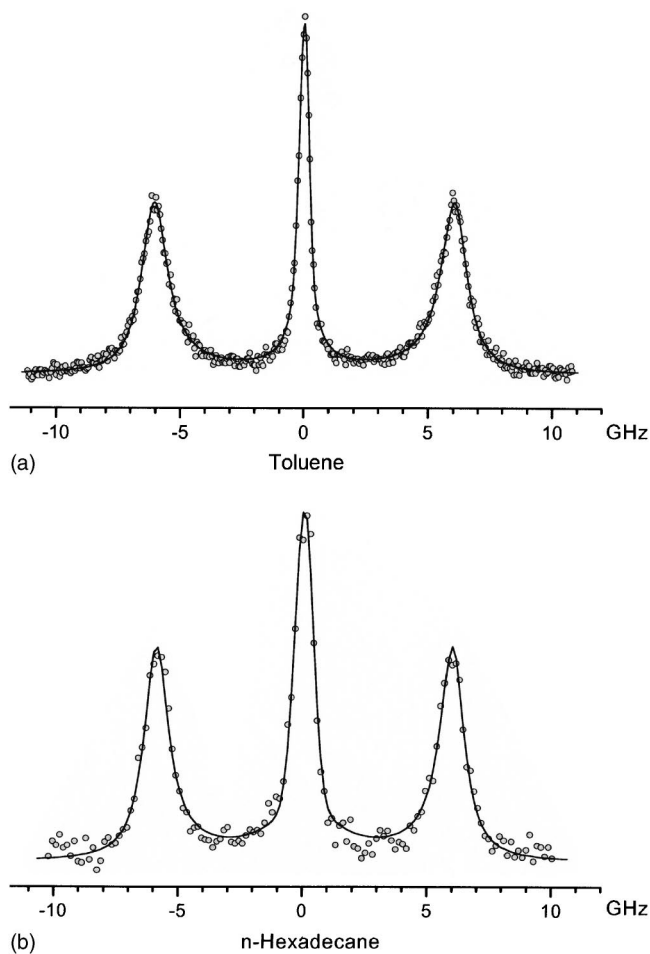


FIG. 8. Brillouin spectra of toluene and *n*-hexadecane at room temperature measured using single-mode fiber detection.

Fig. 9, we compare measurements of a PEO-1K sample in the melted state at a temperature of $T=60\text{ }^{\circ}\text{C}$, with $\lambda=514.5\text{ nm}$ excitation and a scattering angle of $\theta=90^{\circ}$ done by using both the fiber-optic and the conventional pinhole setups. The normalized ACF are represented on a log-time

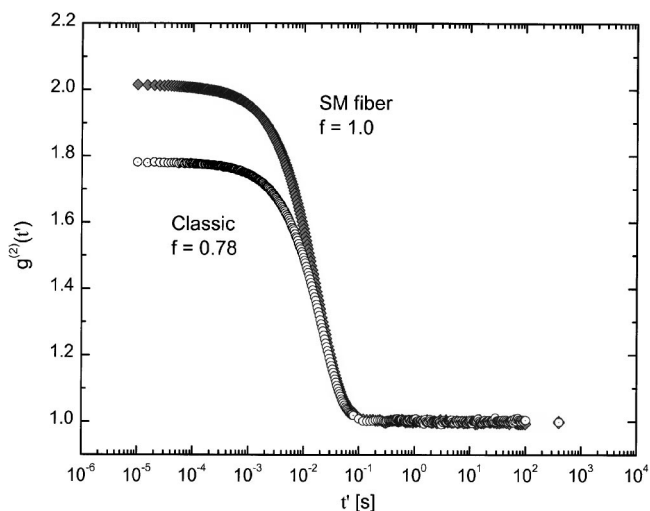


FIG. 9. Classic (circles) vs single-mode fiber-optic (diamonds) light detection used in PCS. The sample was PEO-1 K melt at $T=60\text{ }^{\circ}\text{C}$, scattering angle $\theta=90^{\circ}$, and collection time about 1.5 h; f —coherence factor.

shift plot which has the advantage of providing easy comparison of the relaxation rates. On the graph, the function represented by open circles was taken using the classical setup with a 50 μm diameter pinhole. In fact, it was selected among many measurements because of the very good value of its coherence factor, $f_{\text{pinhole}} \approx 0.78$. The second ACF, represented on the graph by filled diamonds, was measured using the single-mode fiber setup and showed a coherence factor of $f_{SM \text{ fiber}} = 1.0$, in excellent agreement with the prediction. Both ACFs were collected with 1.5 h accumulation time.

In order to extract the coherence factor and the rest of the parameters from the experimental data, we used Kohlrausch–Williams–Watts (KWW) fits, also known as “stretched exponential” fits¹⁸

$$g^{(2)}(t') = 1 + \frac{A}{B_0} e^{-2(q^2 D t')^\beta}, \quad (13)$$

with fitting parameters: A —amplitude, B_0 —baseline, $\Gamma = q^2 D$ —relaxation rate, and β —dispersion parameter, $0 < \beta \leq 1$. The dispersion parameter provides a measure of the width of the distribution of decay rates, Γ . A β value of 1 corresponds to single-exponential relaxation. Smaller values of β indicate broader distributions. In our analysis, the parameter β was always very close to 1. The coherence factor was calculated from the KWW parameters

$$f = \frac{A}{B_0}. \quad (14)$$

One can also use the graph and visually compare the amplitudes of the ACFs. It is evident that the ACF measured using the single-mode fiber setup converges to an intercept of 2 for small values of t' . At the same time, the one taken with the conventional (pinhole) setup converges to a somewhat lower intercept of about 1.8. Both ACFs contain essentially the same information—they show a single exponential relaxation (very narrow distribution) with a matching relaxation rate.

The results in Fig. 9 are comparable to the best results reported in the works of Rička, *et al.*^{3,4} and Suparno *et al.*¹² For example, in Ref. 4, the authors report PCS measurements of dilute suspension of polystyrene latex spheres obtained with fiber-optic detectors with various fiber core diameters. In the case of the single-mode fiber, they report an experimental coherence factor $f = 0.982$. In a second example, in Ref. 12, the authors compare PCS results obtained with a 100 μm pinhole and with a single-mode fiber detector. The sample was again a dilute suspension of polystyrene latex

spheres. The reported coherence factors are $f = 0.673$ and $f = 0.863$, respectively, for the 100 μm pinhole and the single-mode fiber.

Our findings demonstrate that the fiber-coupled setup performs as well as or better than the classical F–P interferometers and PCS spectrometers. At the same time, it provides a great amount of flexibility and convenience in the experiment. A compact detection end allows easy and robust alignment, along with the possibility for angle dependent F–P measurements. The instrument end affords the ability to switch between various spectroscopic instruments without disturbing the experimental conditions and the alignment.

ACKNOWLEDGMENTS

It is a pleasure to thank the U.S. DOE (Office of Basic Energy Sciences) Grant No. DE-FG03–00ER15052, UNLV, and the Bigelow Foundation for financially supporting this work. In addition, the authors thank A. Sanchez, W. O'Donnell, and J. Kilburg for technical support. They also thank R. Pecora and G. Patterson for providing additional components for the F–P interferometer as well as for valuable discussions.

¹For example, see www.oceanoptics.com

²R. Brown, *Appl. Opt.* **26**, 4846 (1987).

³J. Rička, *Appl. Opt.* **32**, 2860 (1993).

⁴T. Gisler, H. Rüger, S. U. Egelhaaf, J. Tschumi, P. Schurtenberger, and J. Rička, *Appl. Opt.* **34**, 3546 (1995).

⁵G. Pakulski and F. Holuj, *Rev. Sci. Instrum.* **61**, 1390 (1990).

⁶M. Born and E. Wolf, *Principles of Optics*, 6th ed. (Pergamon, New York, 1980).

⁷J. M. Vaughan, *The Fabry-Perot Interferometer: History, Theory, Practice, and Applications* (Adam Hilger, Bristol, 1989), and references therein.

⁸G. D. Patterson, *Rayleigh–Brillouin scattering in Polymers*, Methods of Experimental Physics Vol. 16A (Academic, New York, 1980), pp. 170–204.

⁹B. Berne and R. Pecora, *Dynamic Light Scattering* (Dover, Mineola, NY, 2000).

¹⁰H. Cummins and E. Pike, eds., *Photon Correlation and Light Beating Spectroscopy* (Plenum, New York, 1974).

¹¹B. Chu, *Laser Light Scattering* (Academic, New York, 1974).

¹²Suparno, K. Deurloo, P. Stamatelopoulos, R. Srivastva, and J. C. Thomas, *Appl. Opt.* **33**, 7200 (1994).

¹³S. M. Lindsay and I. W. Shepherd, *J. Phys. E* **10**, 150 (1977).

¹⁴R. Walter, R. Walkenhorst, M. Smith, J. C. Selser, G. Piet, and R. Bogoslovov, *J. Power Sources* **89**, 168 (2000).

¹⁵R. Walter, J. C. Selser, M. Smith, R. Bogoslovov, and G. Piet, *J. Chem. Phys.* **117**, 417 (2002).

¹⁶Y. Kato and G. A. Zdasiuk, *J. Opt. Soc. Am.* **65**, 995 (1975).

¹⁷J. E. Rubio, V. G. Baonza, M. Taravillo, J. Núñez, and M. Caceres, *J. Chem. Phys.* **115**, 4681 (2001).

¹⁸R. Kohlrausch, *Ann. Phys. (Leipzig)* **12**, 393 (1847); G. Williams and D. C. Watts, *Trans. Faraday Soc.* **66**, 80 (1970); K. L. Ngai, C. H. Wang, G. Fytas, D. L. Plazek, and D. J. Plazek, *J. Chem. Phys.* **86**, 4768 (1987).